# Efficient Method for the Computation of Lightning Current Distributions in Wind Turbine Blades using the Fourier Transform and the Finite Element Method

A.A.M. Laudani, L. Carloni, O.T. Thomsen, P.L. Lewin, I.O. Golosnoy

IET Science, Measurement & Technology, DOI: 10.1049/iet-smt.2019.0343

# Efficient Method for the Computation of Lightning Current Distributions in Wind Turbine Blades using the Fourier Transform and the Finite Element Method

A.A.M. Laudani[1*], L. Carloni[2], O.T. Thomsen[3], P.L. Lewin[1], I.O. Golosnoy[1]

[1] The Tony Davies High Voltage Laboratory, School of Electronics and Computer Science, University of Southampton, University Road, Southampton, SO17 1BJ, United Kingdom
[2] PolyTech Lightning A/S, Hovedgaden 451K, Hedehusene, 2640, Denmark
[3] Bristol Composite Institute (ACCIS), Department of Aerospace and Engineering, University of Bristol, University Walk, Bristol, BS8 1TR, United Kingdom
[*]a.a.m.laudani@soton.ac.uk

**Abstract: Rotor blades of large, modern wind turbines are susceptible to lightning strikes. In order to produce a design that resists lightning strikes, it is crucial to simulate lightning current propagation in the blade components. Since the current in the blade is generated by the superposition of potential and induced electric fields, a coupling exists between electric and magnetic fields which needs to be calculated by an imposed integral constraint at each time step. Commercial software packages are able to deal with such constraints, but it results in time-consuming computations. Therefore, this work aims to develop a numerical methodology able to compute the voltage which drives the lightning current through the structure. In this way, the problem is reformulated as a voltage-driven one which in turn allows a simple subsequent coupling of electric and magnetic problems. The computation of the voltage waveform was accomplished using the Fast Fourier Transform (FFT) and the Finite Element Method (FEM) to compute the structure impedance in the frequency-domain. The developed procedure showed high efficiency for a blade subjected to different lightning impulses. It allows a description of the time-dependent lightning current to be given, as well as the distribution of current within the blade conductors.**

## 1. Introduction

Over more than a decade, several studies [1] [2] [3] [4] [5] have shown that wind turbine blades are highly susceptible to downward lightning strikes, as well as to triggering upward lightning. Consequently, it is required to equip them with a Lightning Protection System (LPS) capable of preventing damage due to lightning direct attachment. LPSs are composed of metal receptors placed over the blade surface and metal down conductors located in the cavity of the blade. The former are aimed to intercept the lightning leaders, whereas the latter are intended to conduct the lightning current from the attachment point to the earthing system [6] [7]. The receptors have to be designed according to the guidelines and procedures specified in the IEC standard [7]. In this case, most of the lightning energy is discharged to the ground through the LPS [3] [5].

The ever-increasing demand for wind turbines with higher rated power outputs led to the need for longer rotor blades. To meet these requirements and to maintain a low weight, wind turbine manufacturers implemented Carbon Fibre Reinforced Polymer (CFRP) materials into the rotor blade load-carrying laminates, i.e. the spar caps (Fig. 1) [8] [9]. However, the incorporation of a poorly conducting material like CFRP (with conductivity between 3 and 5 orders of magnitude smaller than metals) introduces additional challenges for the protection of the blade against lightning strikes. For instance, equipotential connections need to be realised between the down conductor and the CFRP structure to prevent internal arcs due to a high potential difference between the two conductors, which would cause severe structural damage to the spar cap [10].

The performance of LPSs is mainly assessed by

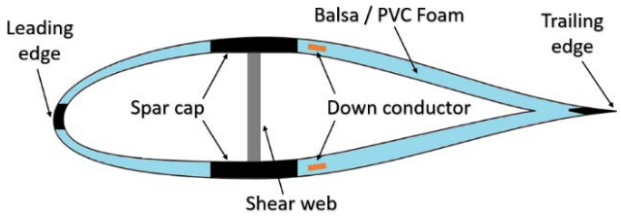


***Fig. 1.*** *Typical wind turbine blade cross-section* [9].

expensive testing, which can cost up to €100,000 including material and manufacturing costs [11]. Numerical simulations using the Finite Element Method (FEM) might represent a cost-effective and time-efficient alternative to testing in order to assess the capability of lightning protection solutions. In fact, once a model is validated, it can be re-employed several times during the design stage (e.g. it might be needed to modify the geometry or to vary the lightning waveform parameters) at little extra cost [6] [7] [12]. However, past research [12] [13] [14] has shown that electric current distributions within the rotor blade structure (down conductors and CFRP spar caps) are driven by both potential electric field and induced electric field generated by the time-variable magnetic field. Current distributions in the blade structure can be predicted through the solution of the field diffusion problem, i.e. by solving for electric and magnetic potentials and coupling them through an imposed integral constraint on the total transport current. A numerical solution of such a combined problem is complex for fast rising currents such as lightning impulses (large induced electric field) and tests on commercial software packages [15] [16] indicate that multiple iterations at each time step are required to find consistent solutions. Moreover, the computational cost of such analyses is even higher for

high aspect-ratio structures like rotor blades, which require fine meshes for accurate predictions.

On the other hand, better convergence and a smaller computational time would be achieved by imposing a transient voltage boundary condition. The latter allows independent calculations of the potential component of the electric field (and of the associated current density, i.e. $-\sigma\nabla V$) in the magnetic potential problem. However, such voltage waveforms are not known from lightning observation studies. Therefore, the objective of this paper is to develop a numerical procedure able to compute the voltage which drives the sought lightning current through the assessed structure.

The FEM is an effective tool to study the thermal damage experienced by wind turbine blades during a lightning strike. In fact, the advantage of this method is the capability to predict the spatial distribution of the current density in the rotor blade cross-section. This would allow the identification of high current density areas, which might lead to resin decomposition, associated outgassing and delamination within the composite [17] [18]. The considerable reduction in computational time achieved through the proposed procedure would make FEM analyses more efficient to study such phenomena. Alternative approaches based on equivalent circuit modelling are less computationally demanding but cannot provide the spatial distribution of the current density in the blade cross-section.

This paper is structured as follows. Section 2 introduces the modelling framework used in this study, while Section 3 presents details of the numerical methodology when applied to the first positive return stroke lightning impulse. Then, the procedure is applied to a second type of lightning current (i.e. the subsequent return stroke) in Section 4. The results are presented and discussed in Sections 5 and 6. Finally, the conclusion sums up the main points of this paper.

## 2. Modelling Framework

As outlined in the introduction, the numerical solution to lightning current distribution problems is complex due to the integral constraint on the total lightning current. This issue can be removed by a subsequent coupling of the equations for electric and magnetic potentials through transient voltage boundary conditions. However, these voltage conditions depend on the lightning current in a non-linear manner, i.e. they cannot simply be scaled up and down from a single reference case. Consequently, a procedure needs to be devised in order to compute the voltage which results in the sought lightning current.

The first step of the developed approach (Fig. 2) is to compute the spectrum of the lightning current. In the second step, the electromagnetic problem is solved in the frequency-domain in order to determine the voltage related to each component of the lightning current spectrum. This can be easily completed since the problem is linear at each fixed frequency, i.e. voltage and current are directly proportional through the impedance. In the third step, the voltage components are transformed back to the time-domain, obtaining the

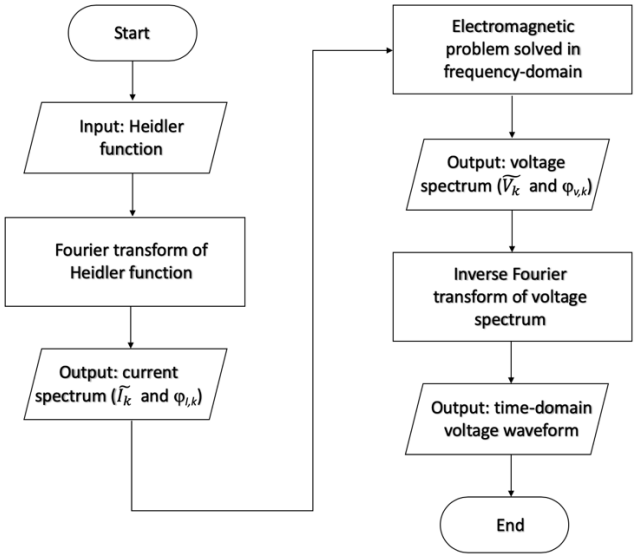


***Fig. 2.*** *Flowchart of the proposed procedure.*

sought transient voltage profile. Finally, the electromagnetic problem is solved in the time-domain applying the determined lightning voltage waveform as boundary condition.

To accomplish this algorithm, the following input data need to be known: *the expression of the transport current to compute its spectrum*; and *the geometry and material properties of the structure under study to evaluate its impedance at different frequencies*. In our application, these are the lightning current and the rotor blade geometry and material properties, respectively.

## 3. Numerical Procedure

The steps outlined in Section 2 are accomplished by the computational algorithms given below. For clarity, the procedure was applied to the first positive return stroke case.

### *3.1. Time-Domain Current: Heidler Function*

The waveforms of lightning short strokes (first and subsequent return strokes given in Table 1) are well approximated by the Heidler function [19] [20]:

$$i(t) = \frac{I_0}{k_0} \frac{\left(\frac{t}{T_1}\right)^{10}}{1+\left(\frac{t}{T_1}\right)^{10}} e^{\left(-\frac{t}{T_2}\right)} \quad (1)$$

where $I_0$ [A] is the peak current, $k_0$ is the correction factor for the peak current (typically around unity), $t$ [s] is the time, $T_1$ [s] is the rise time coefficient and $T_2$ [s] is the decay time coefficient.

Table 2 summarises the Heidler function coefficients [6] [19] [20] [21], while an example of the Heidler function waveform for the first positive return stroke is illustrated in Fig. 3. Note that the time coefficients $T_1$ and $T_2$ that need to be entered in (1) are longer than the standard [7] front duration, $\tau_1$ [s], and time to half value, $\tau_2$ [s], respectively. In fact, the inherent shape of the Heidler function presents an initial offset interval, $T_{off}$ [s], in which the current is zero (Fig. 3).

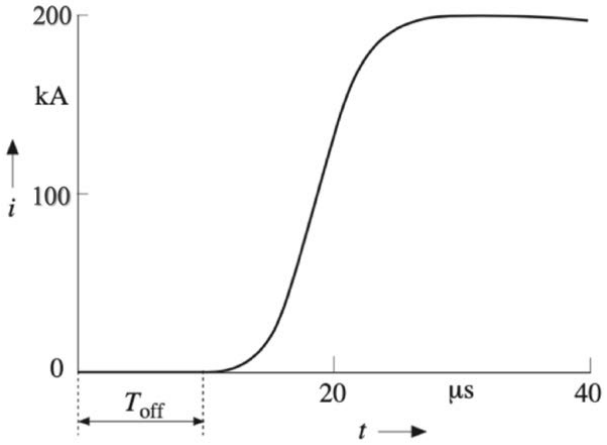


***Fig. 3.*** *First positive return stroke current waveform and offset time* [20].

The first positive return stroke is characterised by a specific energy (i.e. action integral $\int i^2\,dt$) equal to 10 MJ/Ω and consequently it generates a large amount of Joule heating in the structure. Noting this, the downward positive lightning is often considered to assess the Joule heating damage at the equipotential connections between the LPS and CFRP spar [7].

### *3.2. Fourier Transform*

The Heidler function in (1) is composed of two terms with very different time coefficients: the *rise term*, which is a power curve; and the *decay term*, which is the exponential decay. The Fourier integral of (1) cannot be analytically calculated, and the spectrum of the standard lightning waveform can be determined by either numerical integration or the Discrete Fourier Transform (DFT) [20]. The latter is the preferred method since it is more efficient when performed using the Fast Fourier Transform (FFT) algorithm, provided that the total number of samples is an integer power of 2 [22].

The DFT converts a discrete time periodic signal (an array of time-domain samples) into a sum of sinusoidal components (an array of frequency-domain components) [22] [23]. Since the standard lightning current is a non-periodic continuous function, it is first required to sample it. This was done by choosing an appropriate sampling interval, $T$ [s], and number of samples, $N$, to ensure that the sampling reflects the characteristics of the lightning waveform. The observation time, $T_s$ [s], is then defined as [22] [23]

$$T_s = NT \tag{2}$$

whereas the frequency points are defined as

$$f_k = \frac{k}{T_s} = \frac{k}{NT}, \qquad k = \overline{0, N-1} \tag{3}$$

where $k$ is the frequency index (bin number).

The discrete spectrum of the Heidler function is given by the following equation:

$$\widetilde{I_k} = I_k\, e^{j\,\varphi_{I,k}} = \frac{1}{N}\sum_{n=0}^{N-1} i_n e^{-j2\pi\frac{k}{N}n} \tag{4}$$

where $\widetilde{I_k}$ [A] is the frequency-domain $k$-th current complex coefficient, $I_k$ [A] is the magnitude of the $k$-th current complex coefficient, $j$ is the square root of -1, $\varphi_{I,k}$ [rad] is the argument of the $k$-th current complex coefficient, $i_n$ [A] is the $n$-th current sample in the time-domain and $n$ is the time sampling index.

The total number of frequency components is equal to the number of time-domain samples. According to the Nyquist Theorem [22], the frequency bandwidth is half the sampling frequency, $F_s$. Consequently, all the frequency components larger than $F_s/2$ will be aliased when the signal is transformed back to the time-domain. Therefore, when performing the Discrete Fourier Transform of non-periodical signals, the sampling frequency must be chosen carefully in order to prevent significant errors. In addition, special attention should also be paid to [22]

- The selection of the sampling interval, which is chosen to represent the high frequency components of the Heidler function. For this reason, at least 20 time points need to be placed along the rising front. Such an empirical approach allows to pass the "knee" on the current magnitude plot given in Fig. 4a, as well as to ensure that the magnitudes of the aliased components are small enough to be ignored.
- The number of samples, which defines $T_s$ as given in (2) and is chosen to capture the slow decaying tail of the Heidler function, i.e. the current $i(T_s)$ should decay below $10^{-18}$ of its peak value. This is a very conservative requirement and can be relaxed for lightning waveforms that present shorter tails. However, such an excessive extension of the observation time does not affect the computational time of the DFT since it is performed using the FFT algorithm (FEM simulations are instead stopped at 2 ms, which is the typical duration of a lightning short stroke [7]).

An adequate representation of the first positive return stroke was achieved when the sampling interval was 0.61 μs, the number of samples was equal to 32,768 and the frequency bandwidth was ~800 kHz (see Fig. 4a and Fig. 4b). This discretisation is compared in Section 5 with the one employed in [24]. The latter presents computations with only 14 points on the rising front and the current $i(T_s)$ decays to $10^{-6}$ of its peak value.

**Table 1.** Waveform parameters of both the first positive return stroke and subsequent return stroke [7].

| Lightning Impulse | Peak Current $I_0$ [kA] | Front Duration $\tau_1$ [μs] | Time to Half Value $\tau_2$ [μs] |
|---|---|---|---|
| First Positive Return Stroke | 200 | 10 | 350 |
| Subsequent Return Stroke | 50 | 0.25 | 100 |

**Table 2.** Heidler function coefficients for the first positive return stroke and subsequent return stroke [6] [19] [20] [21].

| Lightning Impulse | Peak Current $I_0$ [kA] | Correction Factor $k_0$ | Rise Time $T_1$ [µs] | Decay Time $T_2$ [µs] |
|---|---|---|---|---|
| First Positive Return Stroke | 200 | 0.93 | 19 | 485 |
| Subsequent Return Stroke | 50 | 0.993 | 0.454 | 143 |

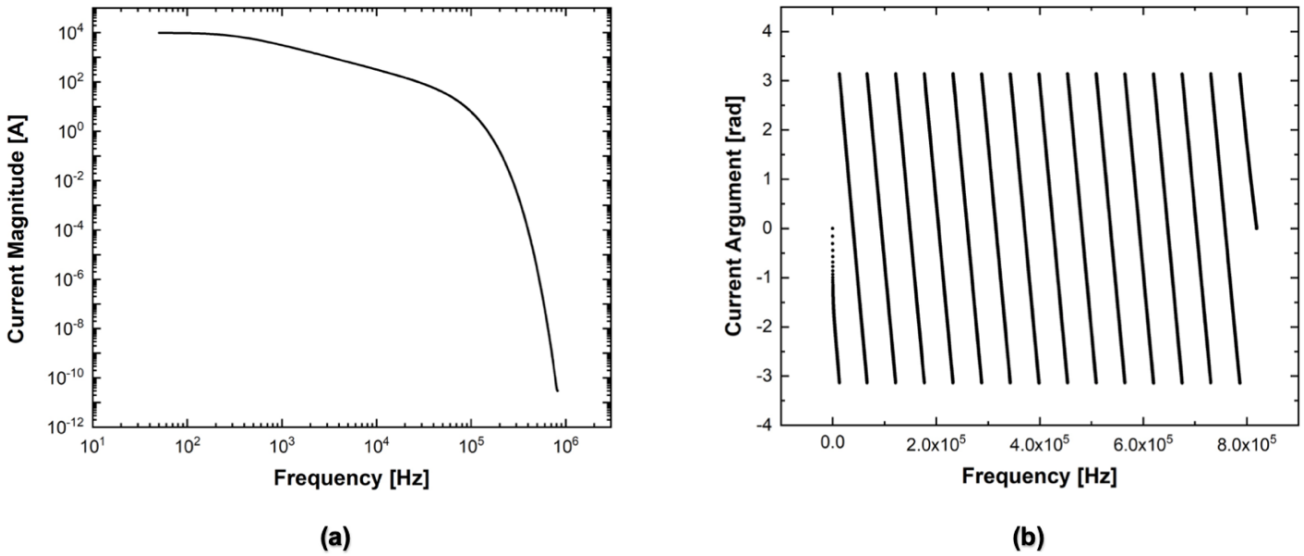


***Fig. 4.*** *First positive return stroke current spectrum:* ***(a)*** *magnitude;* ***(b)*** *argument.*

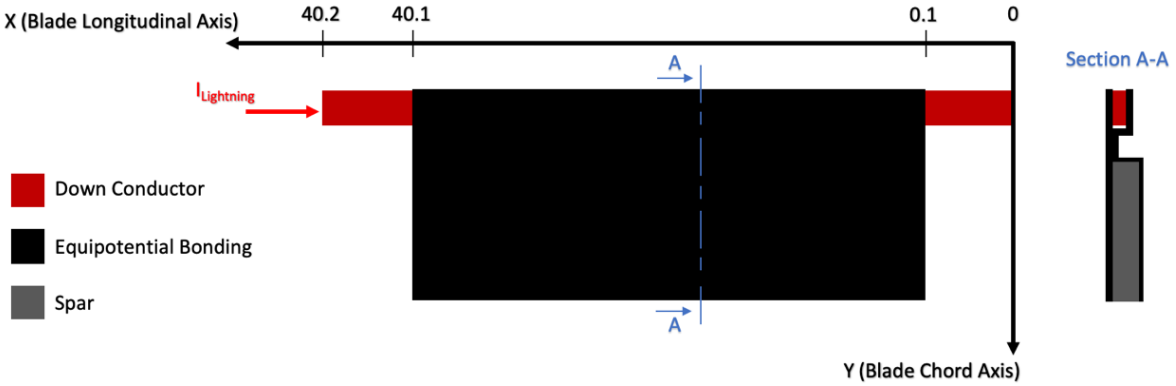


***Fig. 5.*** *Arrangement of the blade conductors (not to scale).*

**Table 3.** Wind turbine blade dimensions [11].

| | |
|---|---|
| **Spar cap** | |
| **Width [mm]** | 400 |
| **Thickness [mm]** | 0.8-27 |
| **Length [m]** | 40 |
| **Spar - Down Conductor Distance [mm]** | 100 |
| **Equipotential Bonding** | |
| **Width [mm]** | 522.8 |
| **Thickness [mm]** | 0.214 |
| **Length [m]** | 40 |
| **Down Conductor** | |
| **Width [mm]** | 22.8 |
| **Thickness [mm]** | 2.2 |
| **Length [m]** | 40.2 |
| **Cross-Section [mm²]** | 50 |

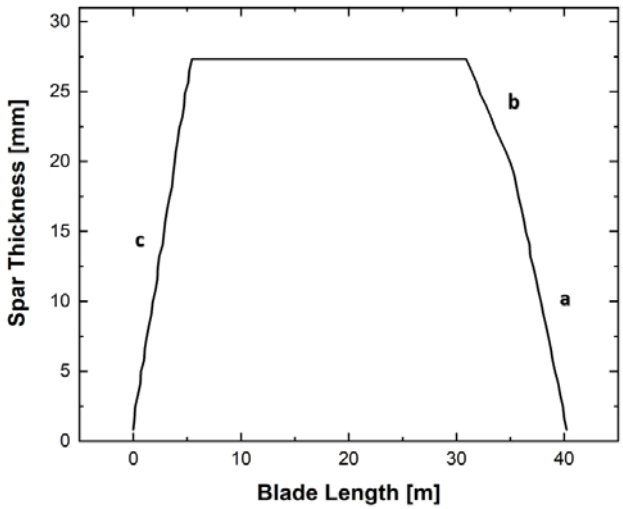


***Fig. 6.*** *Variation of the spar thickness as a function of the blade position* [11].

**Table 4.** Spar, equipotential bonding and down conductor electrical conductivity tensors. The electrical conductivity of both UD and Biax CFRP along the principal directions were experimentally measured in this study using the methodology published in [25] [26] [27]. The CFRP principal directions given in the table are: 1 – along the fibres; 2 – transverse to the fibres; 3 – through-thickness. Biax CFRP is assumed to be approximately in-plane isotropic (1, 2). The conductivity of the copper braid is taken from [11].

| **Materials** | $\sigma_{11}$ **[S/m]** | $\sigma_{22}$ **[S/m]** | $\sigma_{33}$ **[S/m]** |
|---|---|---|---|
| UD CFRP (Spar) | 36380 | 17.910 | 3.950 |
| Biax CFRP (Equipotential Bonding) | 20702 | 20702 | 8.340 |
| Copper (Down Conductor) [11] | $5.998 \times 10^7$ | $5.998 \times 10^7$ | $5.998 \times 10^7$ |

### *3.3. Impedance Calculation: Frequency-Domain Field Diffusion Problem*

Once the spectrum of the transport current is determined, the next step is to predict the voltage spectrum (i.e. the voltage magnitude and phase related to each frequency component of the current spectrum). This was done by solving the steady-state problem in the frequency-domain using the FEM. In order to do so, it was essential to know the geometry and material properties of the analysed system (i.e. the wind turbine blade).

#### 3.3.1. Model Formulation

The rotor blade was modelled in Comsol Multiphysics and the following set of equations were solved in the frequency-domain [15] [16]:

$$\begin{cases} \nabla \times \boldsymbol{H} = \boldsymbol{J} \\ \nabla \cdot \boldsymbol{A} = 0 \\ \nabla \cdot \boldsymbol{J} = 0 \end{cases} \tag{5}$$

while the following relations are known as follows:

$$\begin{cases} \boldsymbol{B} = \nabla \times \boldsymbol{A} \\ \boldsymbol{B} = \mu_0 \mu_r \boldsymbol{H} \\ \boldsymbol{J} = -\boldsymbol{\sigma} \nabla V - \boldsymbol{\sigma} j \omega \boldsymbol{A} \end{cases} \tag{6}$$

where $\nabla \times$ is the curl operator, $\boldsymbol{H}$ [A/m] is the magnetic field strength, $\boldsymbol{J}$ [A/m$^2$] is the conduction current density, $\nabla \cdot$ is the divergence operator, $\boldsymbol{A}$ [Wb/m] is the magnetic vector potential, $\boldsymbol{B}$ [T] is the magnetic flux density, $\mu_0$ [H/m] is the vacuum permeability, $\mu_r$ is the relative permeability, $\boldsymbol{\sigma}$ [S/m] is the electrical conductivity tensor, $\nabla$ is the gradient operator and $V$ [V] is the electric scalar potential.

The displacement current density term has been neglected in (5) since lightning strikes are considered to be low-frequency applications [17] [18] [28] [29]. For instance, at 800 kHz the displacement current in the composite materials is smaller than the conduction current by 11 orders of magnitude along the fibre direction and by 7 orders of magnitude along the through-thickness direction.

In addition, the rotor blade is considered reflectionless in this modelling approach, which has been proved to be a safe assumption [12].

#### 3.3.2. Rotor Blade Geometry and Material Properties

The geometry of the analysed system is shown in Fig. 5 while its dimensions are summarised in Table 3. The spar cap thickness varies along the blade length and the design includes three chamfered profiles, which are ~5 m in length. As depicted in Fig. 6, the spar thickness increases from 0.8 mm to 20 mm (a) and from 20 mm to 27 mm (b) when moving from the tip towards the centre of the blade. It then decreases again up to 0.8 mm (c) when approaching the blade root. The CFRP spar is connected to the down conductor along the entire length of the blade by means of equipotential connections (Fig. 5). The down conductor has a cross-sectional area of 50mm$^2$ [7].

Table 4 lists the electrical properties of the spar, equipotential bonding and down conductor materials. The anisotropic conductivity of both UD and Biax CFRP materials were experimentally measured according to the procedures available in [25] [26] [27]. Finally, the relative permeability of both copper and CFRP materials was assumed to be equal to 1 [30] [31].

The epoxy system used in the CFRP materials was supplied by Hexion and comprised Hexion RIMR035c epoxy resin and Hexion RIMH037 curing agent. The spar UD non-crimp carbon fabrics and the equipotential bonding Biax non-crimp carbon fabrics were supplied by Saertex and had areal weights of 870 g/m$^2$ and 218 g/m$^2$, respectively. Finally, a copper braid [11] was employed as down conductor.

#### 3.3.3. Mesh

The blade structure (Fig. 5) was placed within a computational domain, i.e. the return path, which was a rectangular box of height and width equal to 1 m and length of 40.2 m. The implemented return path is the one usually employed during tests, in which it is placed at a small distance from the blade sample, generally 1-2 m [11] (on the other hand, it would be required to employ infinite elements for general simulations of lightning strikes to rotor blades).

A mesh convergence study was conducted using the automatic mesh refinement option [15] [16] for two frequency components of the current spectrum: the first one had amplitude and frequency equal to 150 A and 20 kHz, respectively; the second one was characterised by an amplitude of $4.147 \times 10^{-11}$ A and a frequency of 800 kHz. The mesh convergence results for these two frequency components are shown in Fig. 7a and Fig. 7b, respectively. Uncertainties in the driving voltage below 0.5% were found when the solving domain was discretised by ~64,000 prismatic elements, and this mesh was used for the analyses carried out in this study (Fig. 8).

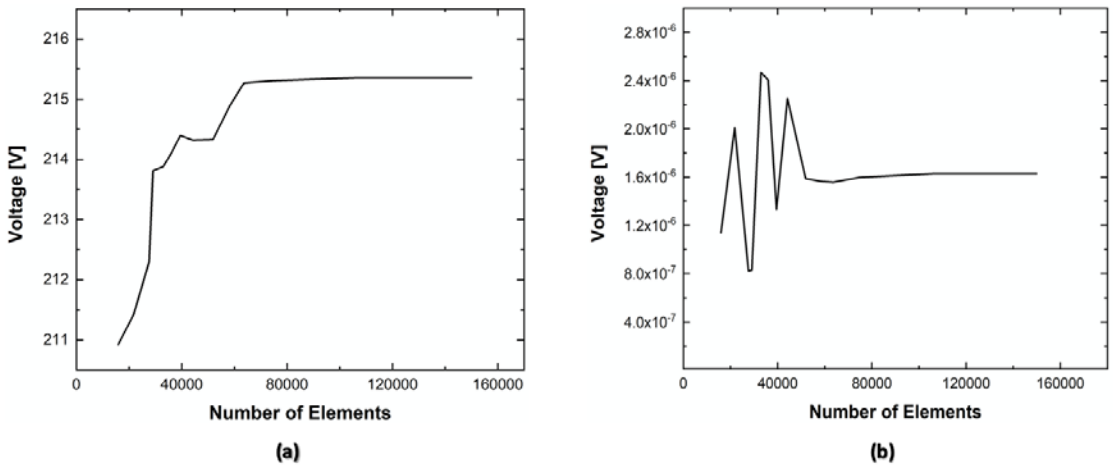


***Fig. 7.*** *Mesh convergence:* ***(a)*** $I_k$ *= 150 A and* $f_k$ *= 20 kHz;* ***(b)*** $I_k$ = 41.47 *pA and* $f_k$ *= 800 kHz.*

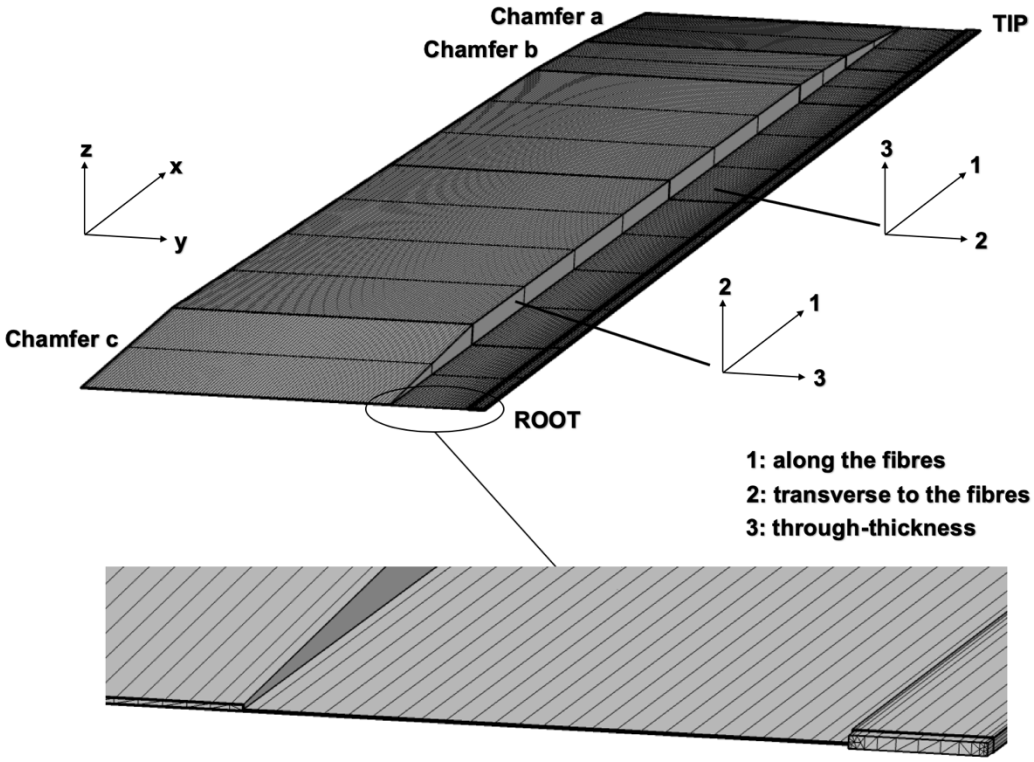


***Fig. 8.*** *FE blade model and mesh implemented in Comsol Multiphysics (the air volume is hidden in this view).*

### *3.4. Selection of Frequency Components and Interpolation Strategy*

As shown in Section 3.2, the typical spectrum of the first positive return stroke current comprised 32,768 components. Solving the electromagnetic problem (in order to predict the voltage components at given frequencies) for all these components is very time-consuming, especially when considering real blade geometries characterised by a high aspect-ratio. Therefore, to reduce the computational time, the electromagnetic problem was solved for a small set of components only, while the remaining voltage components were determined through interpolation.

The selection of the current frequency components for the electromagnetic solution plays an important role in the overall accuracy of the procedure because it might introduce significant errors during the interpolation process. First of all, the electromagnetic problem was only solved for 133 components out of 32,768, which were chosen in such a way as to cover the entire bandwidth of the current spectrum (note that only a small number of components was selected at high frequency, see Fig. 9). The corresponding voltage drops predicted through the FEM were then cubic interpolated to determine the remaining 32,635 voltage components and thus the voltage spectrum (Fig. 10).

However, it is also required to know the phase ($\varphi_{V,k}$) of each voltage component to obtain the required time-domain voltage waveform. Consequently, a second component selection procedure was carried out to determine the voltage phase at different frequencies. To do so, the approximately linear relationship between the current phase and the frequency (Fig. 4b) was exploited. More specifically, a set of frequencies was chosen that lay in all the branches of the bandwidth (Fig. 11). That is, the selected components need to be spaced by approximately $2\pi$ rad. In fact, if the selected

points are spaced by more than 2π rad, then some of the phase branches would be lost. After that, the electromagnetic problem was solved for these frequencies (416 in total) and the corresponding voltage phases are plotted in Fig.12 (blue points). Then, the frequencies at which the phase is minimum (-$\pi$ rad) and maximum ($\pi$ rad) were linearly extrapolated (red crosses in Fig. 12). The phases between the frequencies of minima (-$\pi$ rad) and maxima ($\pi$ rad) were instead determined by linear interpolation, which are given in Fig.13 (blue plot). As a comparison, Fig. 13 also shows the voltage phase obtained when solving the electromagnetic problem in a time-domain computational analysis (red plot) by imposing the transport current, i.e. the slow procedure. A good agreement is obtained between the two, with some discrepancies in the frequency range between 250 and 600 kHz. Because of these discrepancies, it needs to be verified that the correct current is driven by the sought transient voltage (see Section 5).

The performance of the interpolation procedure as a function of the number of selected components is studied in Section 5. The following sets of components were considered for the voltage magnitude and phase interpolations: 20 and 67; 45 and 119; 80 and 294; 133 and 416 (the suggested ones).

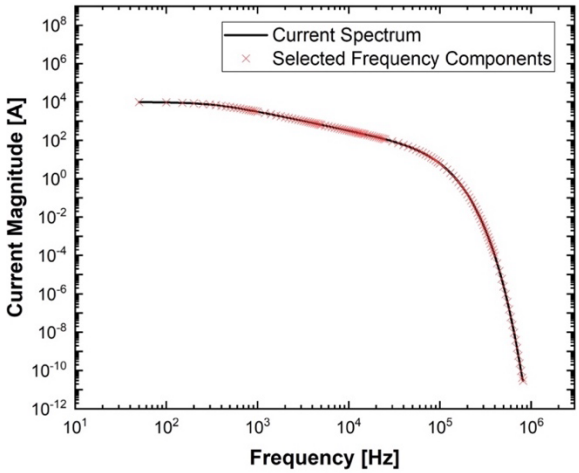


***Fig. 9.*** *First positive stroke: selected current components to determine the voltage spectrum.*

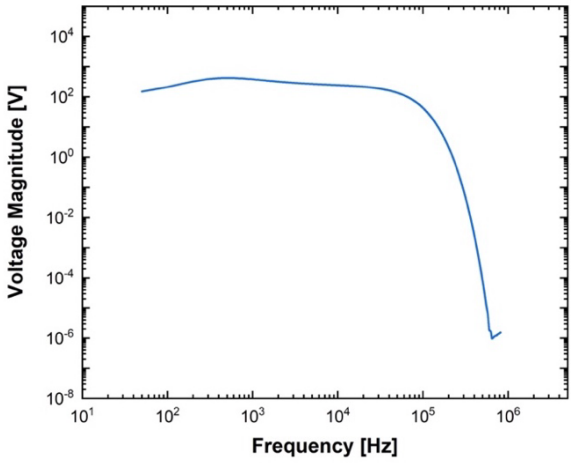


***Fig. 10.*** *First positive stroke: voltage spectrum.*

Finally, it should be noted that the accuracy of the obtained transport current was significantly reduced [24] when only one of the two sets of frequencies (numbering either 133 or 416) was used for both voltage magnitude and phase interpolations (since the two sets are distributed differently within the bandwidth).

### *3.5. Time-Dependent Voltage: Inverse Discrete Fourier Transform*

Once all the frequency components of the driving voltage were found, the voltage spectrum was transformed back to the time-domain using the Inverse Discrete Fourier Transform (IDFT) [22]:

$$v(t_n) = N \sum_{k=0}^{N-1} Re\left(\widetilde{V_k}\, e^{j\,\omega_k\, t_n}\right) = N \sum_{k=0}^{N-1} Re\left(V_k\, e^{j\,\varphi_{V,k}}\, e^{j\,\omega_k\, t_n}\right) \quad (7)$$

where $v(t_n)$ [V] is the time-domain voltage, $t_n$ [s] is the discrete time variable, $\widetilde{V_k}$ [V] is the frequency-domain $k$-th voltage complex coefficient, $V_k$ [V] is the magnitude of the $k$-th voltage complex coefficient, $\omega_k$ [rad/s] is the angular frequency and $\varphi_{V,k}$ [rad] is the argument of the $k$-th voltage complex coefficient.

The resulting time-dependent voltage profile for the first positive return stroke case is depicted in Fig. 14.

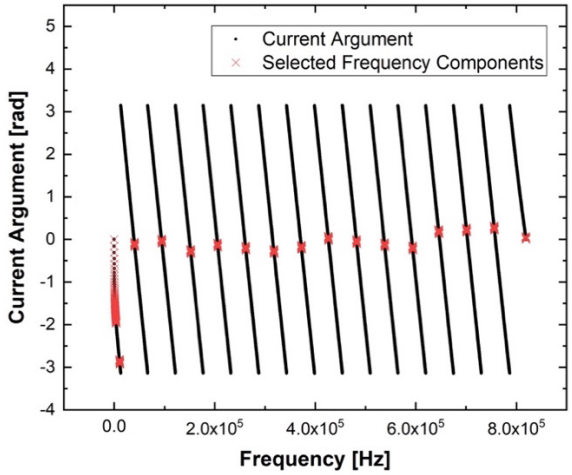


***Fig. 11.*** *First positive stroke: selected current components to determine the voltage phase.*

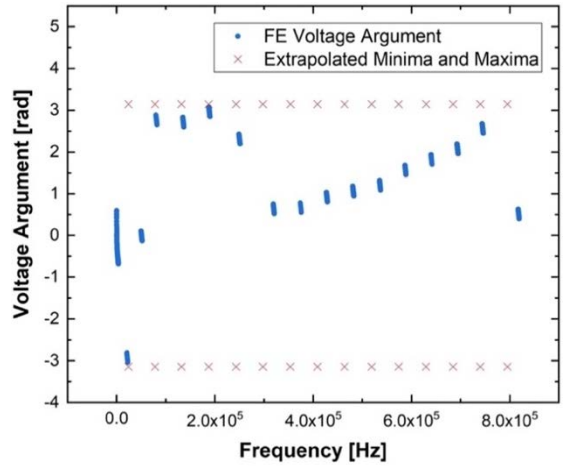


***Fig. 12.*** *First positive stroke: FE voltage phase and extrapolated minima and maxima.*

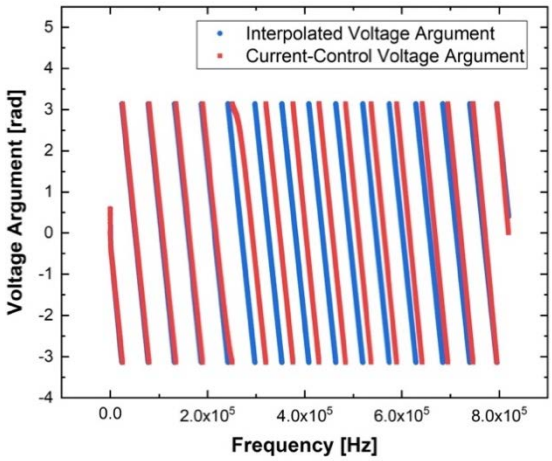


***Fig. 13.*** *First positive stroke: interpolated voltage phase and current-control simulation voltage phase.*

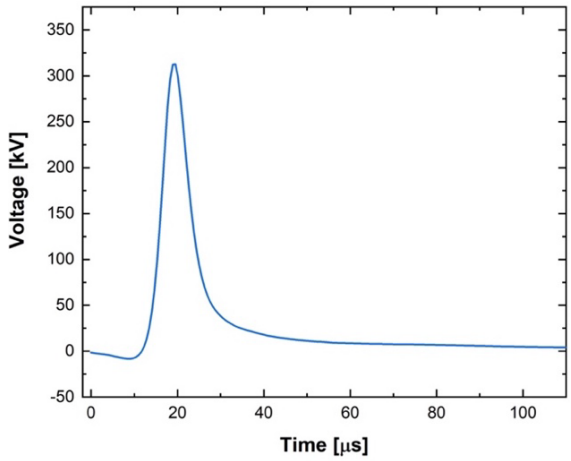


***Fig. 14.*** *First positive stroke: voltage waveform.*

### *3.6. Current Distribution: Time-Domain Field Diffusion Problem*

The sought time-dependent voltage profile determined using (7) was finally applied as a time-dependent boundary condition to solve the electromagnetic problem in the time-domain and compute the associated current distribution within the blade conductors. The equations and boundary conditions are similar to (5)-(6) but in the time-domain formulation [15] [16].

## 4. Second Application: Subsequent Return Stroke

To show the wide applicability of the proposed algorithm, a lightning impulse with faster rising and decay fronts was also considered.

### *4.1. Subsequent Return Stroke Waveform*

The waveform parameters of the subsequent return stroke are listed in Table 1, while the Heidler function coefficients are given in Table 2. Such an impulse presents the largest rate of rise of current, i.e. 200 kA/μs, which will generate the highest voltage drops across the struck structure compared with the other types of lightning strokes. Therefore, this lightning waveform is often used to assess the occurrence of the electrical breakdown of the insulators placed between the down conductor and the CFRP spar [7].

### *4.2. Spectra and Voltage Waveform*

The spectrum of the subsequent return stroke was obtained by choosing a sampling interval of 0.038 μs, 524,288 frequency components and a frequency bandwidth of ~13 MHz (see Fig. 15a and Fig. 15b). Compared with the first positive return stroke, the frequency content of the subsequent return stroke was much larger due to the smaller rise time. Note that it is still valid to neglect the displacement current in (5) under the subsequent return stroke. In fact, at 13 MHz the displacement current in the composite materials is smaller than the conduction current by 9 orders of magnitude along the fibre direction and by 5 orders of magnitude along the through-thickness direction.

Similar to the first positive return stroke case, 154 components were selected (Fig. 16) and interpolated to predict the voltage spectrum (Fig. 17), while 497 were used (Fig. 18) to determine the voltage component phase as a function of frequency (Fig. 19 and Fig. 20). Finally, the sought time-domain voltage waveform for the subsequent return stroke impulse is given in Fig. 21.

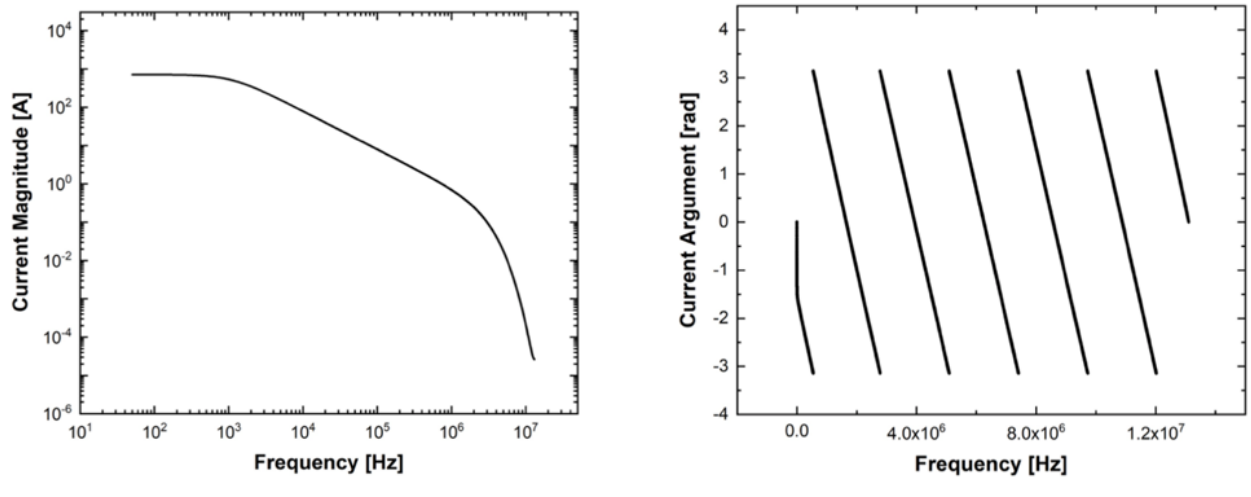


***Fig. 15.*** *Subsequent return stroke current spectrum:* ***(a)*** *magnitude;* ***(b)*** *argument.*

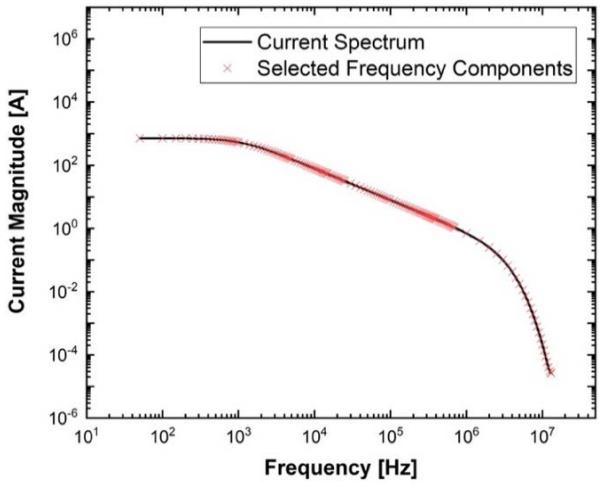


***Fig. 16.*** *Subsequent return stroke: selected current components to determine the voltage spectrum.*

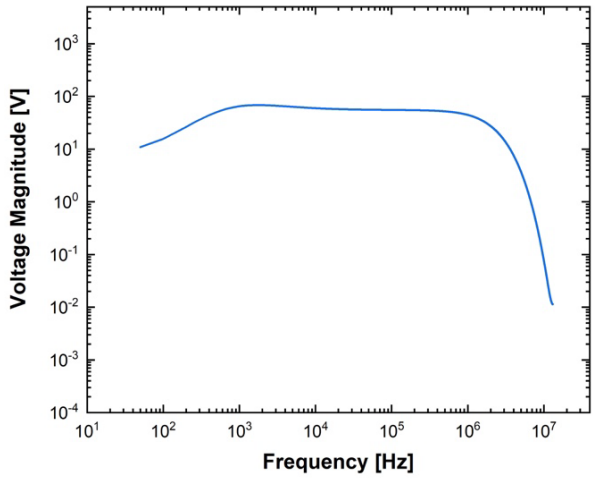


***Fig. 17.*** *Subsequent return stroke: voltage spectrum.*

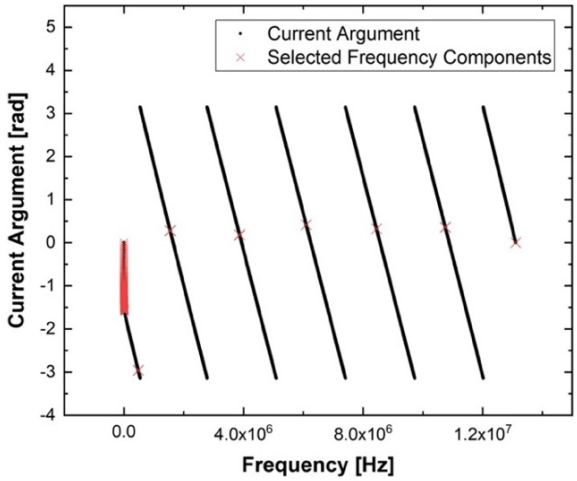


***Fig. 18.*** *Subsequent return stroke: selected current components to determine the voltage phase.*

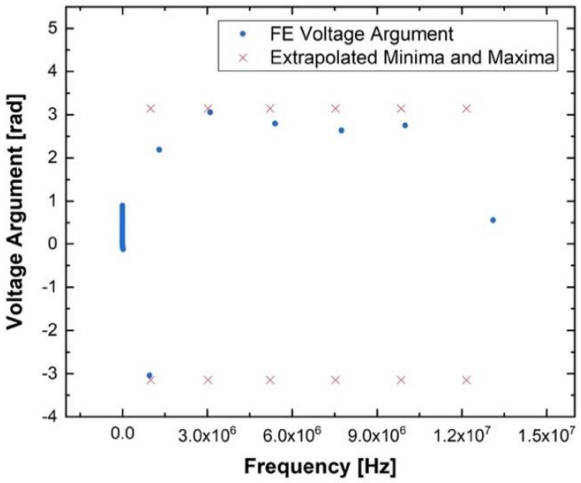


***Fig. 19.*** *Subsequent return stroke: FE voltage phase and extrapolated minima and maxima.*

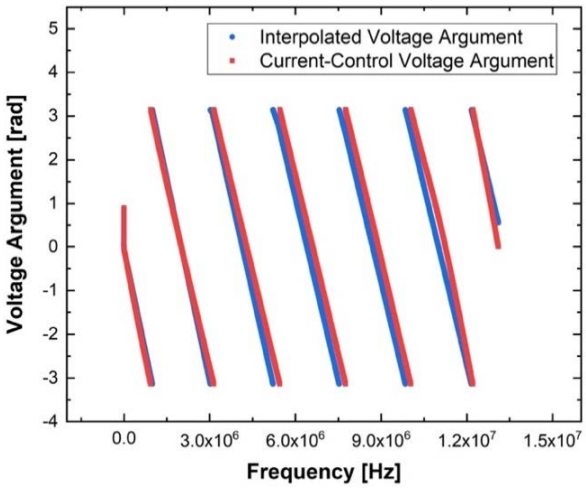


***Fig. 20.*** *Subsequent return stroke: interpolated voltage phase and current-control simulation voltage phase.*

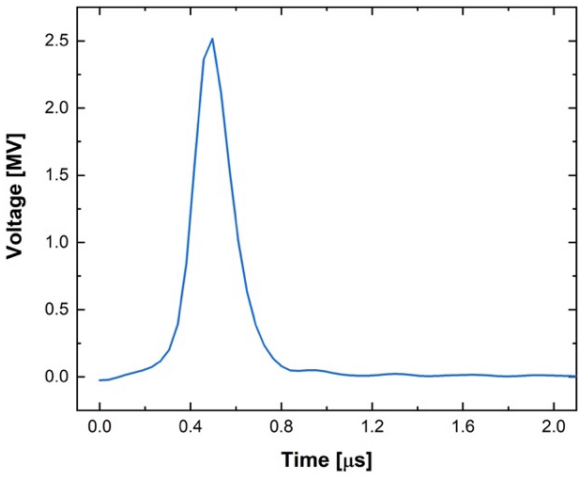


***Fig. 21.*** *Subsequent return stroke: voltage waveform.*

## 5. Results: Predicted Current Waveforms vs Heidler Function

It is required to verify whether the voltage waveforms (Fig. 14 and Fig. 21) computed using the proposed discretisation and interpolation procedures are capable of driving the Heidler function through the rotor blade structure. To this end, the currents injected at the tip of the blade (current density integrated over the down conductor cross-section at $x$ = 40.2 m) were compared to the Heidler function representing the expected lightning currents.

Excellent agreement was obtained between the injected currents (solid green lines) and the Heidler

function (dashed black lines) for both the first positive return stroke (Fig. 22) and the subsequent return stroke (Fig. 23). In the case of the first positive return stroke, slight discrepancies were observed in the rise time, which is delayed by ~3 μs. However, the decay front is fully captured, and the total specific energy of the injected current is equal to 9.955 MJ/Ω, whilst the corresponding Heidler function first positive stroke specific energy is 10.275 MJ/Ω. Similar results were also obtained for the subsequent return stroke, although small discrepancies were found in the value of the current peak, which is overestimated by ~1.5 kA. As a result, the specific energy is also slightly overestimated and equal to 0.185 MJ/Ω, while the Heidler function of the subsequent return stroke has a specific energy of 0.180 MJ/Ω. The negligible differences between the injected currents and the Heidler function are caused by small errors made during the extrapolation and interpolation process of the voltage phase (see Fig. 13 and Fig. 20).

As shown in Fig. 22, the discretisation procedure used in [24] resulted in a rough description of the first positive return stroke current (solid yellow lines). In fact, the initial offset interval preceding the rise front was lost and the current peak was overestimated. In addition, the long decay front was not adequately captured. From these results it appears that 14 points on the rising front and the decay of the current $i(T_s)$ to $10^{-6}$ of its peak value are not sufficient for a correct representation of the Heidler function.

Fig. 24 compares the injected current waveforms calculated by the different sets of selected components used for the interpolation procedure. A low number, e.g. 20-67 (solid red lines) and 45-119 (solid blue lines), resulted in significant oscillations during the initial offset interval, as well as the decay rate was slower than expected. Initial oscillations disappeared as the number of components was increased to 80-294 (solid yellow lines), although an initial negative current was observed. However, correct rise and decay fronts were obtained when employing the suggested interpolation strategy, i.e. 133-416 components.

The total computational time required for the presented examples was 46.6 hours when employing a desktop computer equipped with Intel® Core™ i7-6700 @ 3.4 GHz CPU, 16.0 GB RAM and NVIDIA GeForce GTX 1050 graphics card. Overall the developed procedure is approximately two times faster than the time-domain computations with the imposed transport current. The expected time savings are even greater because a range of different lightning impulses needs to be analysed, i.e. first positive return stroke, first negative return stroke and subsequent return stroke, as required by the IEC 61400-24 Ed.2 standard [7]. In this

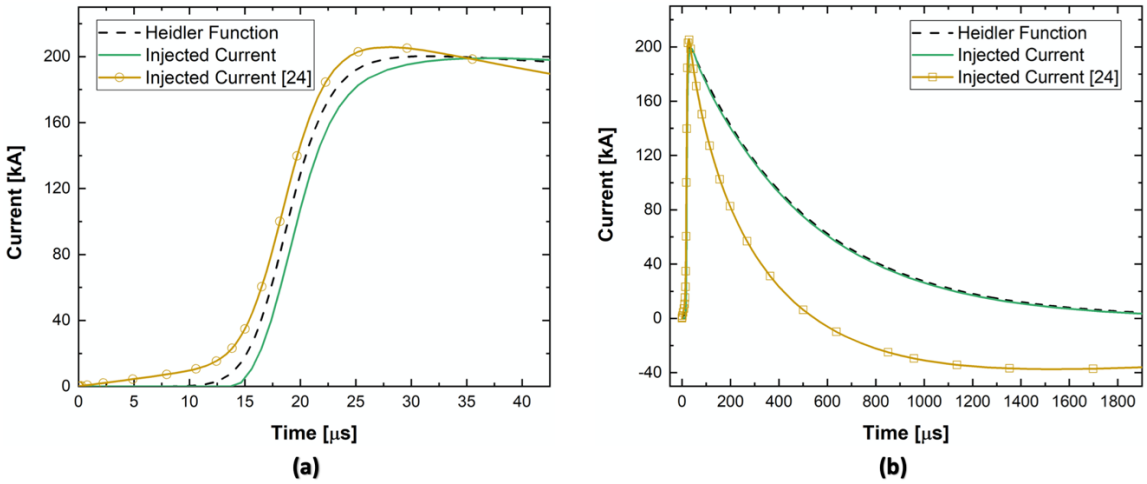


***Fig. 22.*** *Effect of the discretisation procedure for the first positive stroke current:* ***(a)*** *rise front;* ***(b)*** *decay front.*

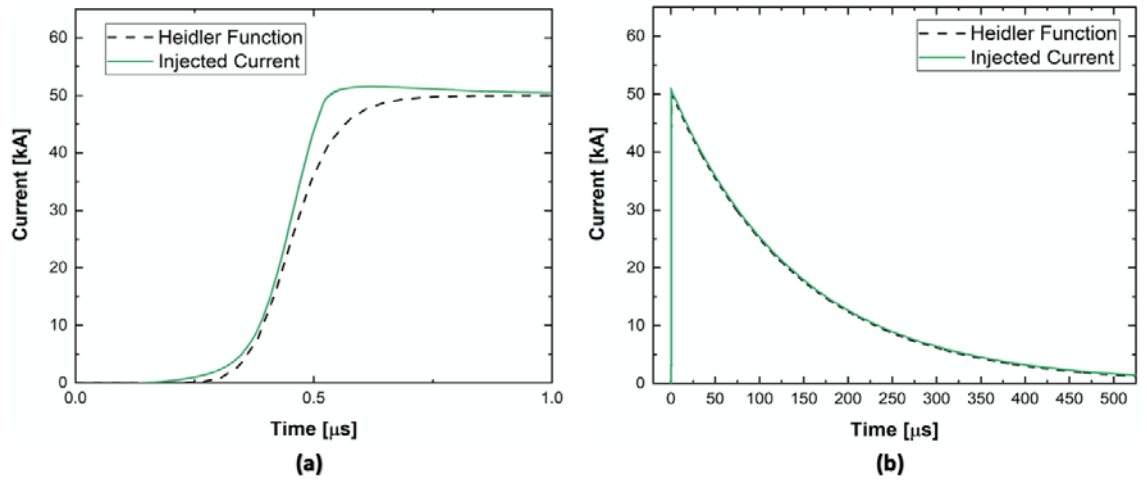


***Fig. 23.*** *Subsequent return stroke injected current:* ***(a)*** *rise front;* ***(b)*** *decay front.*

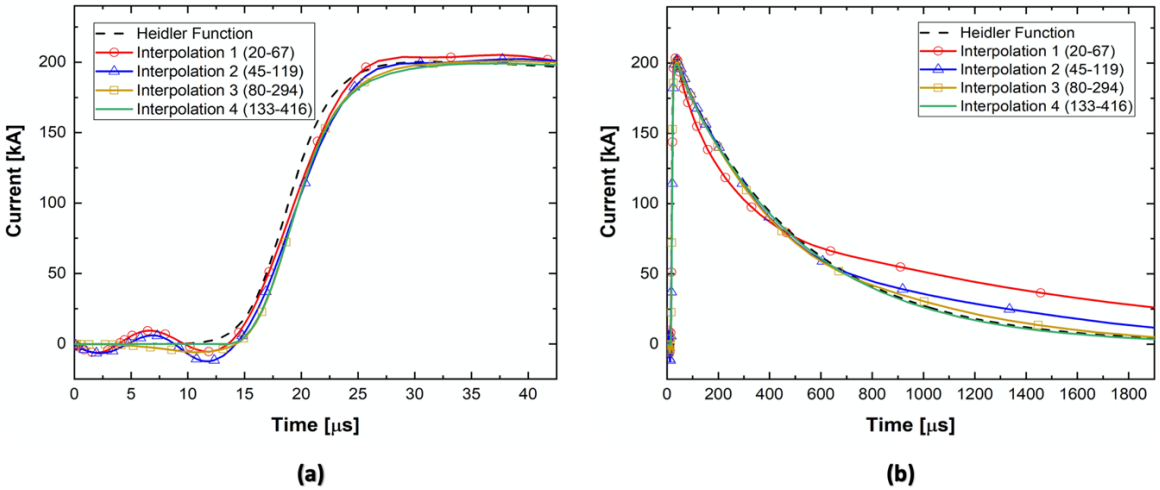


***Fig. 24.*** *Effect of the interpolation procedure for the first positive stroke current:* ***(a)*** *rise front;* ***(b)*** *decay front.*

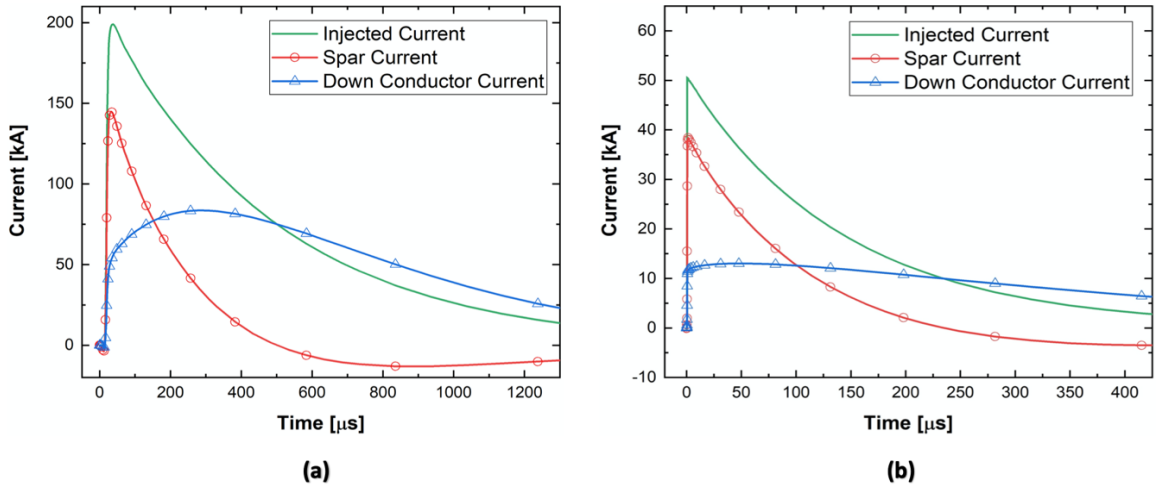


***Fig. 25.*** *Current split between the blade conductors:* ***(a)*** *first positive return stroke;* ***(b)*** *subsequent return stroke.*

case, the expected gain for the whole analysis would be a factor of six since the calculation of the frequency dependent impedance, which is the most time-consuming part of the procedure, would need to be performed only once.

## 6. Discussion

The procedure is capable of predicting the current split between the down conductor and the spar, as shown in Fig. 25a (first positive return stroke) and Fig. 25b (subsequent return stroke). The down conductor currents (blue lines) and the spar currents (red lines) are obtained by integrating the current densities over the cross-section at $x$ = 20 m (i.e. in the middle of the blade). The results show that during the rise front the lightning current is mainly conducted by the spar because of its low inductance, whereas during the slow decaying tail the lightning current mainly flows through the down conductor due to its low resistance. In addition, negative values of current through the spar (reversed currents) are typically observed during testing [11] and are predicted by the present models (see Fig. 25).

Spatial current density distributions within the blade cross-section were computed by the developed numerical models. The distribution in the down conductor cross-section at $x$ = 40 m (Fig. 26a) and $x$ = 33 m (Fig. 26c) reveals that the skin effect (current crowding [32]) is prominent in this component because of the high electrical conductivity of copper. Since the current in the down conductor is mainly localised at its corners, only small contact areas are established with the equipotential bonding layers to divert the current and direct it towards the spar. This results in high current density areas at the bottom equipotential bonding layer within approximately the first 7 m of the blade, i.e. from $x$ = 40 m to $x$ = 33 m (compare Fig. 26b and Fig. 26d).

The electrical conductivity of the spar CFRP is much lower than the electrical conductivity of copper. Thus, no skin effect is observed in the spar although a slight increase in current density is still noticeable at its edges (see Fig. 27a and Fig. 27c). Regions with high current density are instead found in the vertical edge of the top equipotential bonding layer within approximately the first 0.5 m of the blade, i.e. from $x$ = 40 m to $x$ = 39.5 m (compare Fig. 27b and Fig. 27d).

The identified areas of large current density might generate high temperatures because of Joule heating, leading to resin pyrolysis, associated outgassing and delamination inside the composite. Therefore, thermal analyses need to be performed to assess the occurrence of thermal damage in the blade structure.

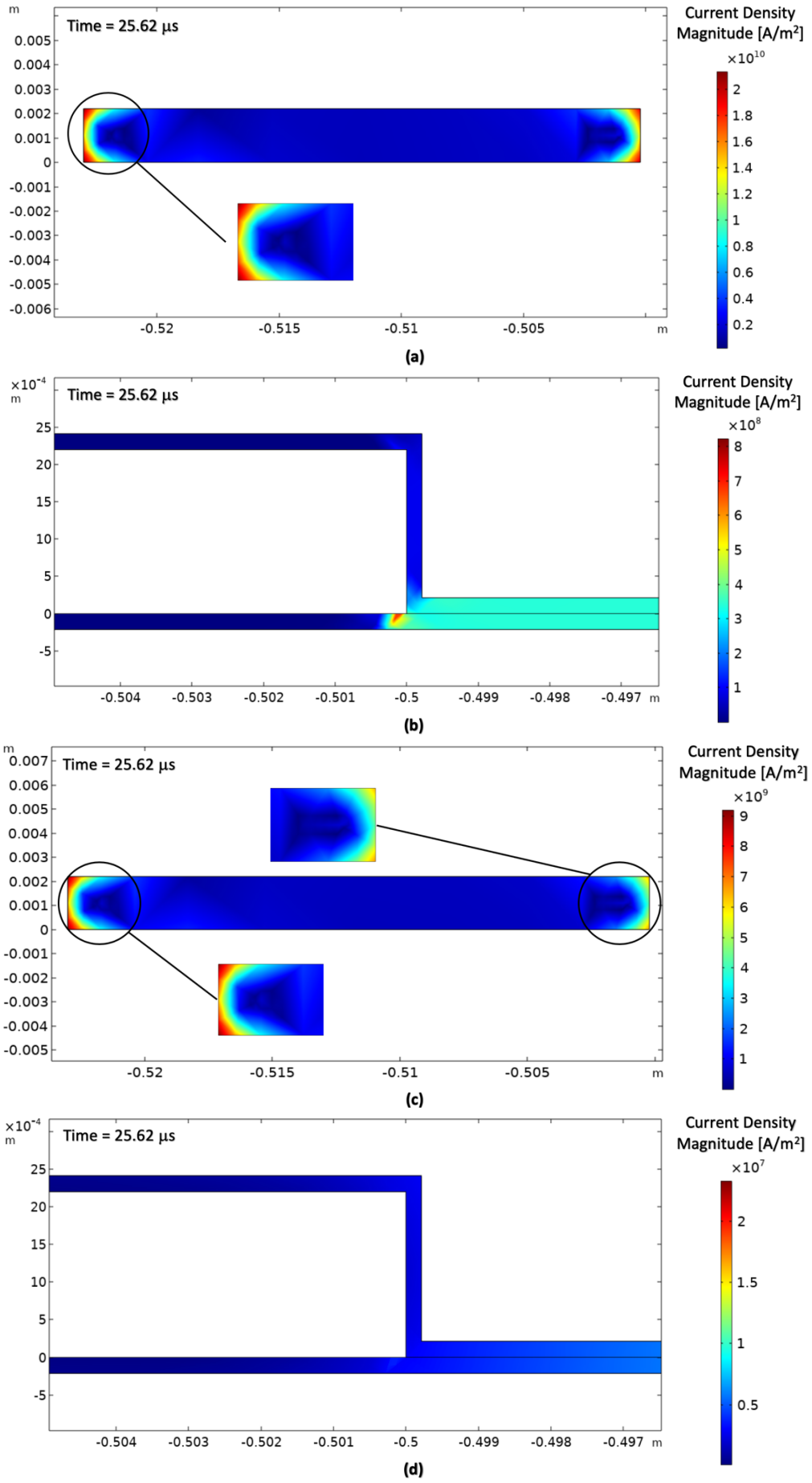


***Fig. 26.*** *Current density distribution under the first positive return stroke:* ***(a)*** *down conductor at x = 40 m;* ***(b)*** *equipotential bonding around the down conductor at x = 40 m;* ***(c)*** *down conductor at x = 33 m;* ***(d)*** *equipotential bonding around the down conductor at x = 33 m.*

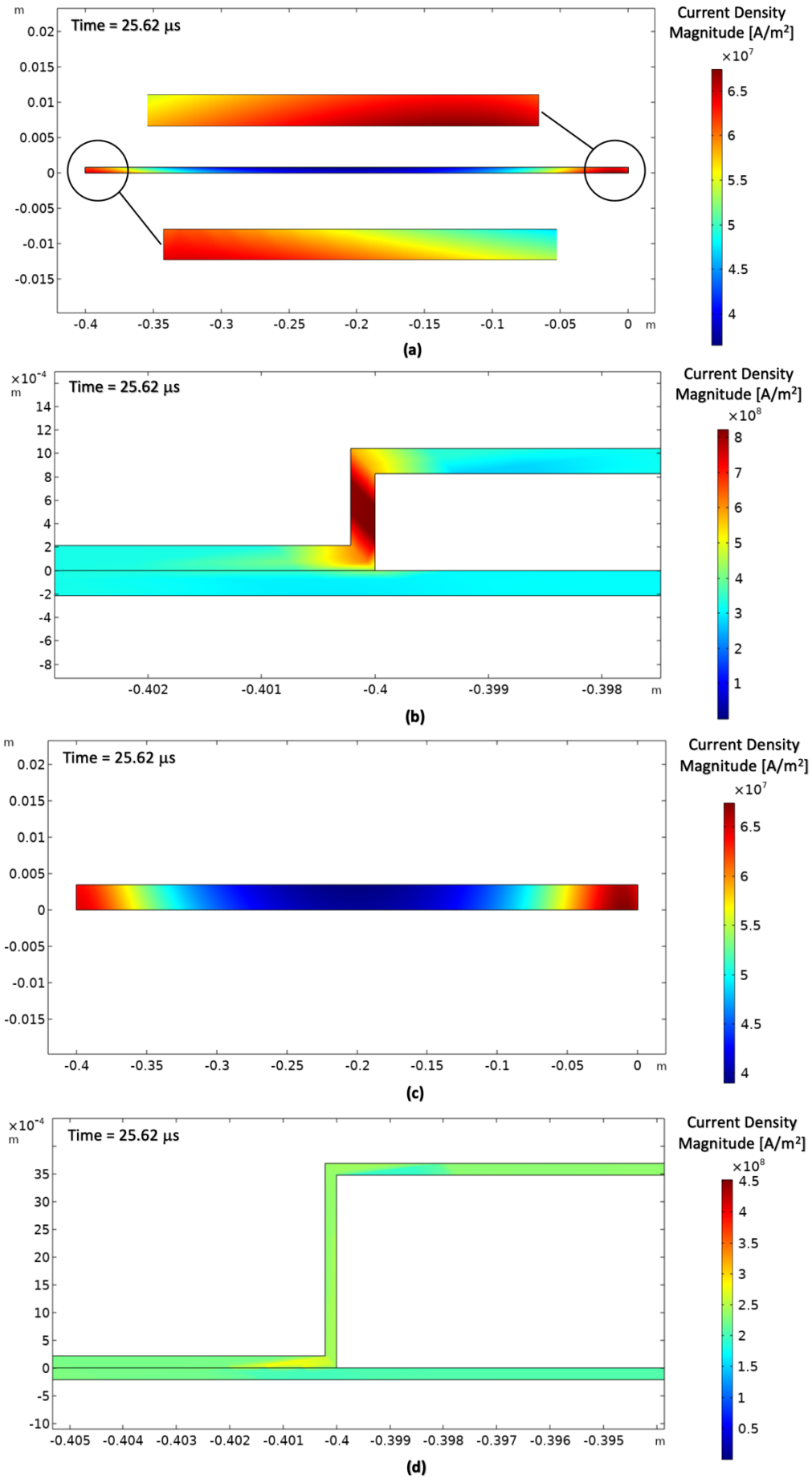


***Fig. 27.*** *Current density distribution under the first positive return stroke:* ***(a)*** *spar at x = 40 m;* ***(b)*** *equipotential bonding around the spar at x = 40 m;* ***(c)*** *spar at x = 39.5 m;* ***(d)*** *equipotential bonding around the spar at x = 39.5 m.*

## 7. Conclusion

This paper presented a numerical procedure able to compute the voltage which drives the lightning current through a wind turbine blade. This was accomplished by first computing the lightning current spectrum and then calculating the blade impedance (and thus the voltage drops across the blade) for a small set of frequencies. After that, the complete voltage spectrum was obtained through interpolation of the predicted voltage-frequency mapping. Finally, the voltage spectrum was transformed back to the time-domain to determine the time-dependent voltage waveform. The simulation of lightning strikes using the voltage driven model was faster than the time-domain calculations with the imposed transport current.

Both the sampling interval and the number of frequency components should be considered carefully for a correct representation of the lightning waveform. The sampling interval should be such as to allow at least 20-time points to be placed along the rising front to represent correctly high frequency components of the Heidler function. On the other hand, the slow decaying tail of the current waveform imposes a requirement on the observation time and thus on the total number of sampling points. It is recommended that the current should drop to $10^{-18}$ of its peak value at the end of the observation. This is a conservative requirement and can be relaxed for lightning waveforms that present shorter tails. However, such an excessive extension of the observation time does not affect the computational time if the FFT algorithm is used. The application of these considerations to two particular lightning impulses showed that the first positive return stroke spectrum could be successfully discretised by 32,768 components, whereas the subsequent return stroke spectrum required 524,288 components. Both discretisation procedures yielded the sought lightning waveforms and specific energies stored in the lightning pulses, although minor discrepancies in terms of rise time and current peaks were observed for the first positive return stroke and subsequent return stroke, respectively.

Finally, the proposed methodology is very generic, and it can be applied to compute the time-domain voltage of any imposed transport current regardless of its waveform, provided that the geometry of the assessed system is known.

## 8. Acknowledgment

This study was funded by the EU Horizon 2020 Marie Sklodowska-Curie Actions - Innovative Training Networks (ITN), SPARCARB project, grant agreement No 642771.

## 9. References

[1] Rachidi, F., Rubinstein, M., and Montanyà, J.: 'A Review of Current Issues in Lightning Protection of New-Generation Wind-Turbine Blades', *IEEE Transactions on Industrial Electronics,* 2008, 55, (6), pp. 2489-2496.

[2] Peesapati, V., and Cotton, I.: 'Lightning protection of wind turbines — A comparison of real lightning strike data and finite element lightning attachment analysis', *International Conference on Sustainable Power Generation and Supply*, Nanjing, China, 2009.

[3] Yasuda, Y., and Yokoyama, S.: 'Proposal of Lightning Damage Classification to Wind Turbine Blades', *7th Asia-Pacific International Conference on Lightning*, Chengdu, China, 2011.

[4] Candela Garolera, A., Madsen, S., Nissim, M., Myers, J., and Holboell, J.: 'Lightning Damage to Wind Turbine Blades From Wind Farms in the U.S', *IEEE Transactions on Power Delivery,* 2016, 31, (3), pp. 1043-1049.

[5] Montanyà, J.: 'Lightning interaction and damages to wind turbines', *V Russian Conference on Lightning Protection*, Saint Petersburg, Russia, 2016.

[6] International Electrotechnical Commission: 'IEC 62305-1 Ed.2.0, Protection against lightning - Part 1: General Principles', 2010.

[7] International Electrotechnical Commission: 'IEC 61400-24 Ed.2.0, Wind Energy Generation Systems - Part 24: Lightning Protection', 2019.

[8] Mishnaevsky Jr, L., Branner, K., Petersen, H., Beauson, J., McGugan, M., and Sørensen, B.: 'Materials for Wind Turbine Blades: An Overview', *Materials,* 2017, 10, (11), pp. 1285-1308.

[9] Brondsted, P., and Nijssen, R. (Eds.): 'Advances in wind turbine blade design and materials' (Woodhead Publishing Limited, Cambridge, 2013), pp. 3-28.

[10] Smorgonskiy, A., Rachidi, F., and Rubinstein, M.: 'Modelling Lightning Current Distribution in Conductive Elements of a Wind Turbine Blade', *International Conference on Lightning Protection*, Shanghai, China, 2014.

[11] Nordex Energy GmbH: 'High Current Test on Wind Turbine Blades' (Internal Report, Unpublished, 2018).

[12] Candela, A., Holboell, J., and Madsen, S.: 'Lightning transient analysis in wind turbine blades', *Proceedings of International Conference on Power Systems Transients*, Vancouver, Canada, 2013.

[13] Nunes de Souza, L., Librantz, H., Amorim, J., and Adabo, G.: 'Analysis of direct effects of lightning on composite structures of aircraft', *IX International Symposium on Lightning Protection*, Foz do Iguacu, Brazil, 2007.

[14] Lepetit, B., Revel, I., Peres, G., Andrivet, L., and Flourens, F.: 'In-strike dynamical measurements of contact resistances', *30th International Conference on Lightning Protection*, Cagliari, Italy, 2010.

[15] COMSOL 5.4: 'AC/DC Module User's Guide', 2018.

[16] COMSOL 5.4: 'Comsol Multiphysics Reference Manual', 2018.

[17] Chemartin, L., Lalande, P., Peyrou, B., et al.: 'Direct Effects of Lightning on Aircraft Structure: Analysis of the Thermal, Electrical and Mechanical Constraints', *Aerospace Lab Journal,* 2012, 9, (5), pp. 1-15.

[18] Chemartin, L., Lalande, P., and Tristant, F.: 'Modelling and simulation of sparking in fastening assemblies', *International Conference on Lightning and Static Electricity*, Seattle, USA, 2013.

[19] Heidler, F., Cvetic, J., and Stanic, B.: 'Calculation of Lightning Current Parameters', *IEEE Transactions on Power Delivery,* 1999, 14, (2), pp. 399-404.

[20] Heidler, F., and Cvetić, J.: 'A Class of Analytical Functions to Study the Lightning Effects Associated With the Current Front', *European Transactions on Electrical Power,* 2002, 12, (2), pp. 141-150.

[21] Djalel, D., Ali, H., and Fayçal, C.: 'The Return-Stroke of Lightning Current, Source of Electromagnetic Fields (Study, Analysis and Modelling)', *American Journal of Applied Sciences, 2007,* 4, (1), pp. 42-48.

[22] Brigham, E.: 'The Fast Fourier Transform and its Applications' (Prentice-Hall, Inc., Englewood Cliffs, 1998).

[23] Orfanidis, S.: 'Introduction to Signal Processing' (Prentice Hall, Inc., Englewood Cliffs, 2010).

[24] Laudani, A., Golosnoy, I., and Thomsen, O.: 'Numerical Computation of Lightning Time-Domain Voltages Using the Fourier Analysis and the Finite Element Method', *Tenth International Conference on Computational Electromagnetics*, Edinburgh, UK, 2019.

[25] Senis, E., Vryonis, O., Golosnoy, I., Dulieu-Barton, J., Thomsen, O., and Madsen, S.: 'The Influence of Graphene Oxide on the electrical conduction in unidirectional CFRP laminates for wind turbine blade applications', *International Conference on Lightning and Static Electricity*, Nagoya, Japan, 2017.

[26] Senis, E., Golosnoy, I., Dulieu-Barton, J., and Thomsen, O.: 'Enhancement of the electrical and thermal properties of unidirectional carbon fibre/epoxy laminates through the addition of graphene oxide', *Journal of Material Science - Composites,* 2019, 54, (12), pp. 8955-8970.

[27] Chippendale, R.: 'Modelling of the Thermal Chemical Damage Caused to Carbon Fibre Composites'. PhD Thesis, University of Southampton, 2013.

[28] Aguilera, P., Lair, C., Issac, F., Michielsen, B., Hélier, M., and Darces, M.: 'Indirect effects of lightning on aircraft engine', *International Conference on Lightning and Static Electricity*, Toulouse, France, 2015.

[29] De Vivo, B., Lamberti, P., Spinelli, G., and Tucci, V.: 'Evaluation of the Lightning Strikes on Carbon Fibers Panels for Aircraft Structural Parts', *Proceedings of Comsol Conference*, Grenoble, France, 2015.

[30] Galehdar, A., Nicholson, K., Callus, P., et al.: 'The strong diamagnetic behaviour of unidirectional carbon fibre reinforced polymer laminates', *Journal of Applied Physics,* 2012, 112, (11), pp. 1-6.

[31] Tzeng, J., and Hsieh, K.: 'Electromagnetic Field Effect and Analysis of Composite Structure', *IEEE Transactions on Plasma Science,* 2015, 43, (5), pp. 1536-1540.

[32] Dwight, H.: 'Skin effect in tubular and flat conductors', *Proceedings of the American Institute of Electrical Engineers,* 1918, 37, (8), pp. 977-998.